Soil & Tillage Research 251 (2025) 106561

Contents lists available at ScienceDirect

Soil & Tillage Research

journal homepage: www.elsevier.com/locate/still

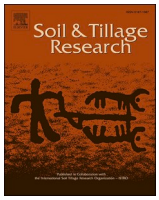

Soil structure development in a five-year chronosequence of maize cropping on two contrasting soil textures

Maxime Phalempin [a,*], Nils Jentzsch [b], John Maximilian Köhne [a], Susanne Schreiter [a], Ralf Gründling [a], Doris Vetterlein [a,c], Steffen Schlüter [a]

[a] Helmholtz Center for Environmental Research (UFZ), Theodor-lieser Straße, 4, Halle (Saale), Sachsen-Anhalt 06110, Germany
[b] Department of Agronomy and Organic Farming, Martin-Luther-University Halle-Wittenberg, Betty-Heimann-Str. 5, Halle (Saale), Sachsen-Anhalt 06120, Germany
[c] Department of Soil Science, Martin-Luther-University Halle-Wittenberg, Von-Seckendorff-Platz 3, Halle (Saale), Sachsen-Anhalt 06120, Germany

ARTICLE INFO

Keywords:
Soil structure
X-ray CT
Root growth
Biopore development
Infiltration capacity

ABSTRACT

The development of soil structure is a complex process driven by the interplay of physical, biological, and chemical factors. Plant roots play an important role in shaping the porous soil architecture; however, their relative contribution is hard to quantify. This study assessed root-driven structural (bio-)pore formation, its impact on hydraulic properties (e.g., infiltration capacity), and how it is influenced by soil texture (loam vs. sand). We combined X-ray computed tomography and machine learning-based segmentation to analyze 720 soil cores from a five-year chronosequence of maize cultivation without tillage. With this methodology, we showed that soil texture was the primary driver of soil structure development and the dynamics of root-derived organic matter. In loam, rapid root decomposition left an interconnected biopore network, enhancing infiltration despite soil settlement. In sand, a greater accumulation of root-derived particulate organic matter resulted from more vigorous root growth, larger diameters, and slower root decomposition. In sand, soil settlement reduced the infiltration capacity over time. These findings underscore the need to integrate organic matter dynamics into soil structure studies, with implications for sustainable land management and carbon storage strategies. Expanding this approach to diverse soils and climates could improve soil process modeling and soil management globally.

1. Introduction

The development of soil structure is a complex process driven by the interplay of physical, biological, and chemical factors. Physical factors play a fundamental role in shaping soil aggregation and fragmentation. For example, fluctuations in moisture and freeze-thaw cycles drive the expansion and contraction of soil cracks (Diel et al., 2019; Leuther and Schlüter, 2021), thus altering the physical arrangement of soil particles. In managed agroecosystems, the applied mechanical forces through tillage or compaction also disrupt soil clods (Or et al., 2021) and change the connectivity of pores (Wardak et al., 2022). Biological factors further modulate the soil structure by fostering aggregation or fragmentation. Soil organisms, such as earthworms, fungi, and bacteria, produce organic residues and excretions that promote the formation of stable soil clods (Redmile-Gordon et al., 2020; Young et al., 1998).

Plant roots are also particularly influential on soil structure through several mechanisms. As they grow into the soil, plant roots may compact the surrounding soil (Phalempin et al., 2021b; Lucas et al., 2019a), which can be assumed to increase soil stability in the vicinity of the roots. They also release root exudates that act as natural binding agents and promote the stabilization of soil clods (Morel et al., 1991). After their decay, plant roots leave well-connected networks of empty channels (biopores), which are known to influence many soil properties, such as water infiltration, air capacity, and gas diffusion (Kautz, 2015; Uteau et al., 2013). This combination of processes initiates positive feedback loops and drastically impacts soil structure and its capacity to support vital ecosystem functions (Rabot et al., 2018).

Modeling soil structure development is a particularly challenging task because the processes that drive soil structure development are closely interconnected (Mueller et al., 2024). For example, microbial activity influences organic matter decomposition, which affects clod stability, while physical processes such as compaction alter microbial habitats (Whalley et al., 1995). Decoupling these processes to improve our mechanistic understanding of soil structure development is likely to result in an oversimplification of their interdependencies. In addition, soils are highly heterogeneous, with varying textures, mineral

* Corresponding author.
E-mail address: maxime.phalempin@ufz.de (M. Phalempin).

https://doi.org/10.1016/j.still.2025.106561
Received 7 February 2025; Received in revised form 21 March 2025; Accepted 24 March 2025
Available online 28 March 2025

compositions, organic matter contents, and biological communities. This variability complicates the development of soil-crop models that directly integrate soil structure dynamics across different environments and land use. Soil-crop models that integrate soil structure dynamics would be significant improvements over current models. They could more accurately represent the time-variable nature of soil hydraulic properties (Sandin et al., 2017), which is known to influence simulation results. However, this time variability is usually neglected in most models (Schwen et al., 2011).

Despite the current challenges, recent modeling efforts have been made in this direction. For example, in the BODIUM model (König et al., 2023), soil structure dynamics is directly integrated by considering physical processes such as tillage (and consolidation thereafter) and the action of plant roots on the creation of biopores with increased vertical continuity. In the approach of Meurer et al. (2020), the volume change of soil phases as a function of time is expressed directly as a function of biological processes such as root growth and decay and the ingestion and egestion of the casts of earthworms. These approaches were successfully applied for the modeling of yield in tilled systems (König et al., 2023) and the recovery of macroporosity following compaction (Meurer et al., 2020; Keller et al., 2021). They pioneered the successful integration of soil structure dynamics in soil-crop models; however, both studies also highlighted the paucity of relevant data on the temporal evolution of soil physical and hydraulic properties for model calibration and validation.

X-ray computed tomography (X-ray CT) is now a well-established imaging method for characterizing soil structure non-invasively. X-ray CT enables the analysis of key soil parameters such as pore connectivity, macroporosity, and pore size distribution (Weller et al., 2022). In combination with novel image processing tools, it also allows the distinction between pores of different origins, i.e., pores created by abiotic factors such as wetting and drying cycles and pores of biotic origin such as pores created by plant roots (Cheik et al., 2021; Lucas et al., 2022). All in all, X-ray CT opens interesting avenues for the study of the impact of root growth and subsequent decay on the dynamics of soil structure. Therefore, it can provide valuable data to complement the aforementioned modeling approaches. However, X-ray CT is constrained by the trade-off between the sample size and the image resolution. This implies that, at the image resolution used to image root tissues of common crops (ranging from 10 μm to 100 μm), the water contained in the porosity of the soil cannot be resolved. As a result, X-ray CT cannot be used to provide relevant hydrological data to feed into soil-crop models.

Notwithstanding the numerous advantages provided by X-ray CT, several challenges arise for the long-term characterization of soil structure with this technology. Among others, the inherent spatial and temporal heterogeneity of soil structural properties is a major constraint. Due to this, the number of samples has to be relatively high, so that the temporal variability is not masked by the spatial variability. An additional constraint can be posed by the differences in the water content of the samples at the time of sampling, which can vary widely from year to year in a given region. In fact, it is recognized that differences in soil water content can influence the results of segmentation and thereby compromise an accurate characterization of soil constituents (Mooney et al., 2012; Hou et al., 2022). This further highlights the need to design powerful image segmentation pipelines that are robust and efficient in dealing with images of different quality.

In the present study, we used advanced techniques such as X-ray CT in combination with machine learning methods for an accurate segmentation of soil constituents. These methods helped us characterize soil structural properties in a continuous five-year chronosequence of soil structure development. In addition, we used more traditional techniques, such as tension infiltrometers, to quantify changes in hydraulic properties over time. The main objective of this study was to characterize the contribution of plant roots to the formation of structural (bio-) pores. In addition, it aimed to assess their influence on hydraulic properties, such as infiltration capacity, and to examine how this influence varies with soil texture.

To achieve this objective, we investigated the unique field experiment of the Rhizosphere Spatiotemporal Organization research program (Vetterlein et al., 2020,2021). This chronosequence was initiated with homogeneously repacked substrates and was managed for five years as a monoculture of maize without tillage. The massive effort required to establish and monitor this field experiment resulted in a rare opportunity to study soil structure development for two contrasting soil textures (a loam and a sand), under the same climatic conditions and with homogeneous initial conditions. This field experiment and methodology aimed to characterize the time required for homogeneously repacked substrates to evolve to a typical soil structure that reflects the given land use. We hypothesized that soil texture is a major driver governing soil structure development through differences in the physical stability of root-induced pores and in the fate of root-derived particulate organic matter (POM). In addition, we hypothesized that the impact of plant roots on the soil structure at the microscale is reflected at the macroscale and can be measured through changes in soil infiltration capacity.

2. Materials and methods

2.1. Field experiment

The field experiment was established in Bad Lauchstädt, Germany (N 51.390424 E 11.875933). During the period 1993–2013, the mean annual precipitation and temperature in Bad Lauchstädt were 525 mm and 9.7 ˚C, respectively (Schädler et al., 2019). The experiment consisted of 24 individual rectangular plots (11 m in length and 3.1 m in width). The plots were excavated to a depth of 1 m and the native soil was replaced with two substrates, a loam and a sand, respectively. The substrate loam (L) was obtained from the upper 50 cm of a haplic Phaeozem soil profile. The substrate sand (S) consisted of a mix of 83 % quartz sand (WF 33, Quarzwerke Weferlingen, Germany) and 17 % of the sieved loam. Table 1 summarizes the textural properties and organic carbon content of the substrates after the establishment of the soil plots.

After soil excavation, the vertical side walls were covered with a root barrier (420 Xavan 420 g m^{-2}, RootBarrier BV, The Netherlands). The plots were then filled by layering 25 cm of gravel under 75 cm of loam or sand. The loam was prepared by sieving it through a heavy-duty double-deck vibrating screen with a 20 mm mesh aperture. After sieving, the loam was placed in 15 cm layers using a wheel loader, leveled with its bucket, and compacted with a 70 kg vibrating plate applying a pressure of 8 N cm^{-2} at reduced speed. For the sand plots, the same method was followed, except that the vibrating plate was omitted. The substrates were compacted to bulk densities of 1.36 g cm^{-3} and 1.50 g cm^{-3} for loam and sand, respectively. Each substrate had twelve replicates, with six plots planted with the *Zea mays* L. B73 *wild-type* (*WT*) genotype and the other six with the corresponding root hair less mutant *rth3* genotype. This created a two-factorial design with the “soil texture” (loam or sand) and “maize genotype” (*WT* or *rth3*) as experimental factors, and with six replicates for each treatment ($n = 6$).

The experiment started in April 2019. During five growing seasons, maize plants were cultivated in the plots each year from April to October. From the end of October until March, the plots were covered with a permeable tarp to prevent weed growth during the non-cultivation period in winter. When there were weeds, they were removed by hand. Maize stubble was left on the plots after harvest.

Table 1
Textural properties and organic carbon content of the substrate sand and loam after establishment of the soil plot. Mean value and standard errors around the mean are given with the notation “mean ± SE” ($n = 12$).

Substrate	Clay [%]	Silt [%]	Sand [%]	C_{org} [%]
Loam	19.5 ± 0.26	47.9 ± 0.17	32.5 ± 0.36	0.85 ± 0.01
Sand	2.6 ± 0.17	5.6 ± 0.35	91.8 ± 0.51	0.15 ± 0.01

Heavy machinery was not allowed to pass over the plots to avoid artificial modification of the soil structure. There was no tillage operation and there was no mechanical disturbance of the soil structure below the first 4 cm. For more information on the field experiment, the reader is referred to Vetterlein et al. (2020, 2021).

2.2. Soil settlement

To assess the degree of soil settlement, the soil surface of four of the 24 plots (two sand and two loam plots) was measured by laser scanning. The measurements were made with a Leica Nova Multistation MS50, which allowed for a high precision of ± 2 mm. The four plots were scanned from the north and south sides up to a distance of 10 m from the scanning device. All data obtained were processed in the geographic coordinate system EPSG 25832 (ETRS 89, UTM zone 32 N) and processed with QGIS (QGIS Development Team, 2023). A permanently installed concrete block was scanned each year to assess the uncertainty of the measurements. Height differences (expressed as elevation above sea level) were measured at the beginning and end of the experiment and once a year in April during the experiment (Table SM1). More information on the procedure for soil settlement measurements is provided in the supplementary information (see section SM1.2).

2.3. Bulk density

Bulk density was measured taking undisturbed soil cores (volume = 250 cm^3), in April 2019 and March 2024 (Table SM1). For the two sampling events, one core per plot was taken at a depth of 10 cm to avoid the surface layer that was disturbed by manual weeding. The dry soil mass was determined after desiccation in a 105 °C oven until a constant weight was reached. The bulk density was expressed on soil dry mass basis, normalized by the total volume of the sample.

2.4. Infiltration capacity

To monitor the development of the infiltration capacity of the plots, infiltration tests were performed with custom-made tension infiltrometers and a setup similar to the one suggested by Ankeny et al. (1991). The infiltrometers had a disc diameter of 20 cm and a reservoir diameter of 7.5 cm. The water infiltration rates were measured on each plot at a tension h = -2 cm and h = − 0.5 cm, at a depth of 10 cm to avoid the surface layer disturbed by manual weeding. We solved the equation of Wooding (1968) for the unconfined steady-state infiltration of water from a circular source to derive water fluxes into the soil. The saturated hydraulic conductivity (K(h = 0 cm)) was then calculated assuming that the hydraulic conductivity decreased exponentially as a function of soil matric potential (Gardner, 1958). More information on this method of calculation is given in the supplementary material SM1.3. Infiltration measurements were performed at the beginning and end of the experiment, and at least once a year (Table SM1).

2.5. X-ray CT

To characterize the evolution of soil structure, undisturbed soil cores were extracted from the field plots and scanned with X-ray CT. The undisturbed soil cores consisted of aluminum rings of 5 cm in diameter and height. They were extracted from each plot at depths of 6.5, 16.5, 26.5 and 36.5 cm (corresponding to the middle of the core) in the same pit between the maize rows. In 2019, the sampling campaigns were carried out in four growth stages, i.e., BBCH14, BBCH19, BBCH59, and BBCH83 according to the German coding of the phenological growth stages of maize (Bleiholder et al., 2001). These stages correspond to the stages of “four fully emerged leaves” (BBCH14), “nine or more leaves unfolded” (BBCH19), “end of tassel emergence” (BBCH59) and “early grain filling” (BBCH83). For the other years, the sampling campaigns were carried out in BBCH19 only, that is, usually at the end of June or beginning of July (Table SM1). This sampling schedule yielded a total of 720 soil cores to analyze. The cores were stored at 4 °C in sealed plastic bags prior to X-ray CT scanning. All cores were scanned within five days after sampling.

X-ray CT scanning was conducted using an industrial μCT scanner (X-TEK XTH 225, Nikon Metrology) equipped with a PerkinElmer 1620 Flat Panel X-ray Detector (1750 × 2000 pixels). The acquired images were reconstructed into 3D tomograms with an isotropic side length of 25 μm and an image depth of 8-bit using a filtered back projection algorithm in CT Pro 3D software (Nikon Metrology). Converting to 8-bit grayscale significantly reduced storage requirements without substantial loss of information. During this conversion, the grayscale range was normalized using a percentile stretching method, with which the darkest and brightest 0.2 % of the voxels were set to 0 and 255, respectively, with linear scaling applied to the intermediate values.

2.6. Image pre-processing

Region of interests (ROI) were carefully defined for each image after visual inspection. The ROIs were drawn to exclude regions close to the core wall where possible soil disturbance had occurred due to sampling. The first and last hundreds of slices of the stacks were also cropped to exclude structure artifacts due to sampling.

To ensure that soil constituents exhibited a consistent gray value throughout the dataset, a series of preprocessing steps were applied to the ROIs. These steps included a histogram mode normalization and corrections for gray value radial and vertical drifts. Mode normalization of the histogram was used to reduce contrast differences between samples, which arose due to the percentile stretching method used during conversion to 8-bit. Radial drift correction normalized gray values across radial distances from the core center to its periphery to correct for beam hardening artifacts. Vertical drift correction standardized gray values along vertical distances from the top to the bottom of the sample, compensating for artifacts caused by the conical X-ray beam of the scanner. All preprocessing steps were performed using the Fiji distribution of the ImageJ software (Schindelin et al., 2012) and custom macros written in ImageJ scripting language.

2.7. Image segmentation

Image semantic segmentation was performed using a supervised machine learning procedure for voxel classification. The method relies on a random forest classification and is implemented in the Labkit plugin (Arzt et al., 2022). Individual classifiers were trained for each soil texture. For both loam and sand, we identified six classes of interest, namely the soil matrix, abiotic pores, living roots, root residues, root-induced empty channels (biopores), and particulate organic matter that is not root-derived (e.g., leaves or seed fragments). Note that for sand, the “soil matrix” class comprised both the sand grains and the sieved loam mixed within the quartz sand. We considered root residues to be root-like objects of which the gray values were lower than those of living roots (possibly due to decay or desiccation) (see section SM1.4 for more information).

Because there were no applications of soil amendments (e.g., litter, straw, crop residues, etc.) on the plots, the POM that is not root-derived originated exclusively from the sieved loam. We included this class in the segmentation scheme as it helped us capture fresh roots with more accuracy. In fact, this differentiation was crucial because both classes generally exhibited a comparable range of gray values, which led to false positives in one class or the other. However, the POM that is not root-derived was not included for further quantitative analysis.

To train the classifiers, ten substacks (1711x1711x300 in dimensions x, y, z, respectively) were selected for each soil texture as representative of the dataset, that is, together they contained all the constituents of interest. The substacks were then concatenated into a single stack and imported into Labkit. Image annotation was performed with test lines on

each material class while avoiding annotating the boundaries of substacks. The annotation of the images was done iteratively until satisfactory segmentation results were achieved, which took approximately 4 h for each soil texture.

The classifiers were designed to extract the original gray value intensity, Gaussian blurs, difference of Gaussian, gradient magnitude, Laplacian of Gaussian, Hessian eigenvalues, variance and structure tensor eigenvalues at sigma levels of 1, 2, 4, 8 and 16. This design allowed us not only to harness the attenuation property of soil constituents but also to leverage their morphological characteristics for more accurate segmentation. These characteristics included the shape (e.g., cylindrical versus planar), the texture (homogeneous versus heterogeneous distribution of gray value within soil constituents), or edges (i.e., transient change in gray value at the border between soil constituents). The resulting classifiers were then applied to all other images in the dataset to segment the grayscale images. It took approximately 40 min to segment a 4 GB image. The computations ran on the GPU (NVIDIA Quadro P4000) of a workstation running on Windows (64-bit, Intel(R) Xeon(R) Gold 6142 CPU and 192 GB RAM).

2.8. Image post-processing

Image post-processing was applied to living roots, root residues, and root-induced empty channels. For post-processing, object fragmentation was reduced by consecutive dilation, holes filling and erosion steps in 3D. In the resulting images, a shape detection filter was applied to isolate cylindrical objects. This filtering step relied on two criteria, the "Vesselness" and the "Size" of the object. More information on this filter and its mathematical formulation is given elsewhere (Phalempin et al., 2021a).

2.9. Quantitative image analysis

Quantitative data from segmented images were derived by computing the diameter of the pores with the Local Thickness plugin (Doube et al., 2010), implemented in ImageJ. The normalized volume of living roots, root residues, and root-induced empty channels was also calculated by summing the number of voxels belonging to these classes and dividing by the total volume of the ROI. Here, we considered bioporosity as the normalized volume of root-induced empty channels.

2.10. Water content measurements

Soil moisture was monitored throughout the experiment with soil water content sensors (TEROS 10; Meter Group AG) (Jorda et al., 2022). Sensors were installed at four depths (10, 20, 40, and 60 cm) within one representative plot for each treatment. To assign a volumetric water content value to each undisturbed core, we assumed that the water content of the undisturbed cores sampled at 6.5 cm depth was the water content measured at 10 cm depth. Following the same logic, we further assumed that the water content of the undisturbed cores sampled at 16.5 and 26.5 cm depth was the water content measured at 20 cm depth, and the water content of the undisturbed cores sampled at 36.5 cm was the water content measured at 40 cm depth. The retained water content values were the ones measured at 9 am on the day of sampling. Because data from soil water content sensors were not available for March 2024, we used the volumetric water content obtained by bulk density measurements. For this, we assumed that the water content of the undisturbed cores sampled at 6.5 and 16.5 cm was the water content measured at a depth of 10 cm.

2.11. Data analysis and visualization

Analysis of output data was carried out in the R environment (R Core Team, 2024). When relevant, differences in median between groups were evaluated using the non-parametric Mann-Whitney U (Mann and Whitney, 1947) (for two groups) or Kruskal-Wallis tests (Kruskal and Wallis, 1952) (for more than two groups). Post-hoc pairwise multiple comparisons were performed after Dunn's methodology (Dunn, 1964) and the p-values were adjusted according to the Benjamini-Hochberg procedure (Benjamini and Hochberg, 2018). When relevant, the results are reported in the text with the notation "mean ± SE" to denote the mean of the distribution and the standard error around the mean. Data visualization and 3D renderings were performed with the ggplot2 package (Wickham et al., 2023) and VGStudio Max (version 3.4, Volume Graphics GmbH, Heidelberg, Germany), respectively.

3. Results

3.1. Evolution of soil settlement and bulk density

During the course of the experiment, the mean elevation above sea level of the plots decreased, clearly indicating a tendency towards soil settlement. This tendency was more pronounced in loam than in sand. In loam, the elevation difference (ΔZ) in March 2024 was equal to −20.2 mm, while it was equal to −7.1 mm in sand (Fig. 1*a*). The elevation of the reference concrete block was stable during the course of the experiment and showed a divergence of −2 mm in height only, after five years (Figure SM1*d*).

The trend toward soil settlement was also confirmed by an increase in bulk density between April 2019 and 2024 (Fig. 1*b*). In loam, the bulk density increased from 1.39 ± 0.015 g cm^{-3} in 2019–1.53 ± 0.053 g cm^{-3} in 2024 ($p = 0.059$, $n = 12$). In sand, the bulk density increased from 1.50 ± 0.009 g cm^{-3} in 2019–1.57 ± 0.015 g cm^{-3} in 2024 ($p < 0.001$, $n = 12$). Interestingly, the standard error around the mean bulk density increased by a factor of 3.5 in loam between 2019 and 2024, while it only increased by a factor of 1.7 in sand. The maize genotype had no effect on the bulk density after five years of cultivation ($p > 0.1$).

3.2. Evolution of infiltration capacity

In sand, the settlement of the plots clearly manifested itself in a gradual decrease in infiltration capacity during the first two years of the experiment before a certain stabilization was reached from October 2021 (Fig. 1*c*). This decrease was even more apparent when comparing the saturated hydraulic conductivities (K_{sat}) in April 2019 and 2024 (Fig. 1*d*). In April 2024, the saturated hydraulic conductivity in sand was reduced by a factor of 2, compared to April 2019, and the difference between the median K_{sat} value was highly significant ($p < 0.001$, $n = 12$). In loam, the effect of soil settlement on infiltration capacity was more evident directly after the first growing season, as it caused a drop in saturated hydraulic conductivity by a factor of 2. After the first growing season, the infiltration capacity gradually and steadily increased. In April 2024, the median K_{sat} value was 1.3 times higher than in April 2019 ($p = 0.25$, $n = 12$) (Fig. 1*d*). The maize genotype had no effect on the saturated hydraulic conductivity after five years of cultivation ($p > 0.1$).

3.3. Bioporosity development

The texture-specific responses of the infiltration capacity with respect to soil settlement could be interpreted with the bioporosity measurements obtained from X-ray CT imaging (Fig. 2). In loam, bioporosity increased at all depths during the course of the experiment ($p < 0.001$) (Fig. 2*a* to 2*d*). The rate of increase in bioporosity (indicated by the slope of the linear regression) gradually decreased with depth. It was 2.37 times higher at 6.5 cm depth compared to 36.5 cm depth. At the end of June 2019, the contribution of bioporosity was only 0.78 % of the total visible porosity. At the end of June 2023, the contribution of bioporosity increased by a factor of 4.6 and reached 3.62 % of total visible porosity (data not shown). Interestingly, the bioporosity values

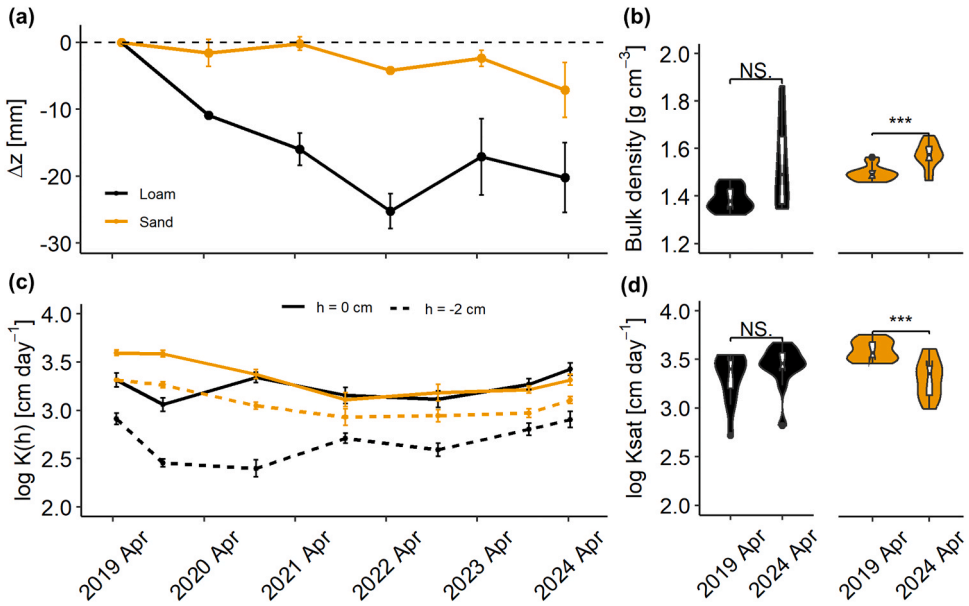

Fig. 1. Development of soil settlement (subfigure *a*) and its impact on bulk density (subfigure *b*) and soil hydraulic conductivity at two matric potentials $h = 0$ cm and $h = -2$ cm (subfigure *c* and *d*) during the course of the experiment. Treatments are differentiated by color (loam in black; sand in yellow), with error bars representing standard error with $n = 12$ for subfigure *b*, *c* and *d*. Significant differences are indicated by the annotations above the violins (*** indicates $p < 0.001$; NS. indicates no significant differences).

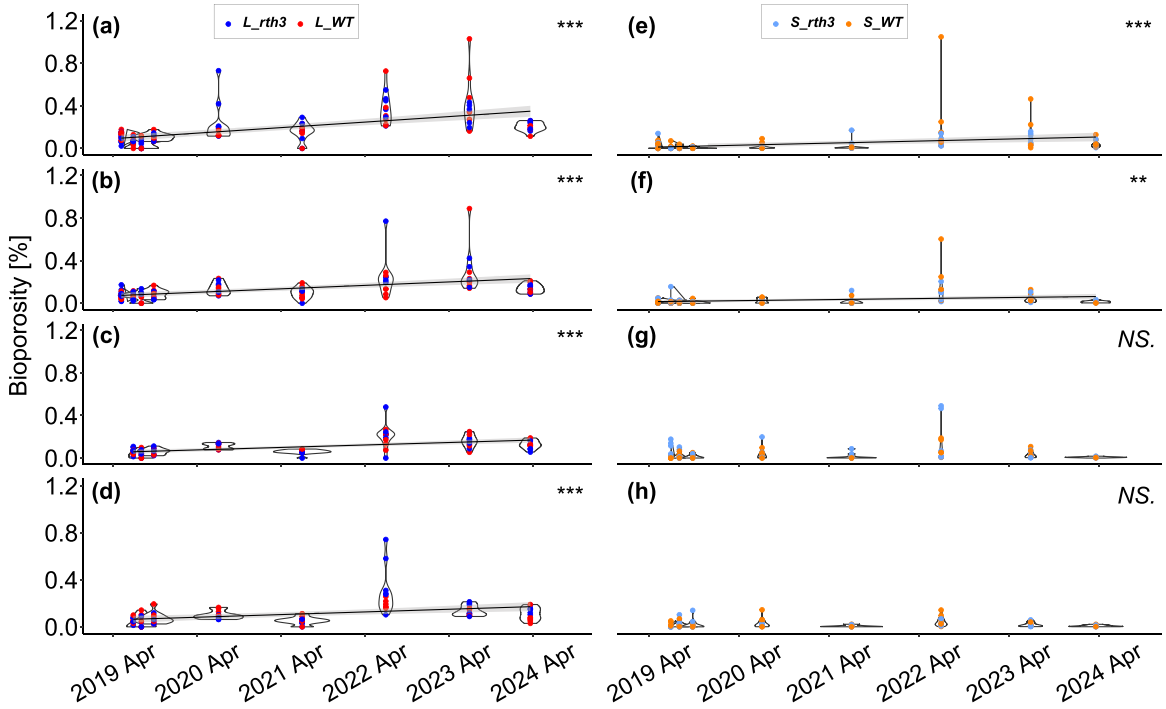

Fig. 2. Time-series of bioporosity during the course of the experiment in loam (subfigures *a* to *d*) and sand (subfigures *e* to *h*). Subfigures are vertically ordered so as to reflect the sampled depths, i.e., *a-e* = -6.5 cm, *b-f* = -16.5 cm, *c-g* = -26.5 cm, *d-h* = -36.5 cm. Each dot represents the value of one measured undisturbed core and the violin plots represent the combined distribution of bioporosity for *WT* and *rth3* at a given sampling event. Treatments are differentiated by color (*L_WT* in blue; *L_rth3* in red; *S_WT* in light blue and *S_rth3* in orange). The stars and letters on the upper right corner of each subfigure indicate the level of significance for the slope of the linear regression of bioporosity with time (*** indicates $p < 0.001$; ** indicates $p < 0.01$; NS. indicates non significant differences).

measured in March 2024 were significantly lower than at the end of June 2023 ($p < 0.05$). In sand, bioporosity only increased at depths of 6.5 and 16.5 cm (Fig. 2*e* to 2*h*). The rate of increase in bioporosity over time was 2.6 and 3.4 times higher in loam than in sand at 6.5 and 16.5 cm depth, respectively. At the end of June 2023, the contribution of bioporosity reached only 0.19 % of the total visible porosity in sand (data not shown). For both sand and loam, there were no obvious differences in bioporosity between the maize *WT* and *rth3* genotypes (data not shown).

The development of bioporosity from the end of June 2019–2023 can be visually appreciated with 3D renderings (Fig. 3*a* to *d*). These subfigures show grayscale 3D transects in the upper part and the biopores

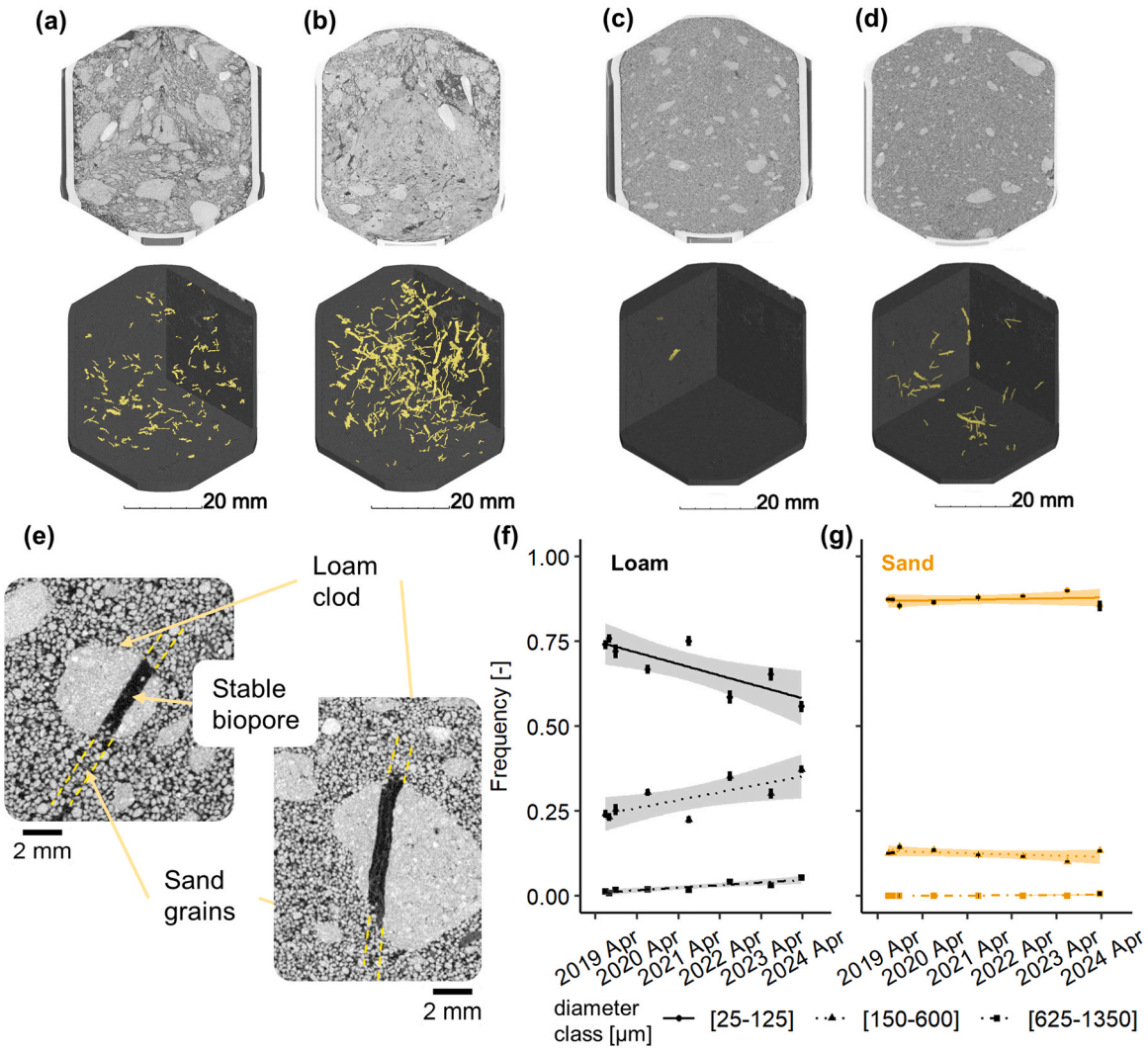

Fig. 3. Bioporosity development and its impact on soil pore size distribution. Subfigures *a-d* show grayscale 3D transects in the upper part and the segmented biopores in the lower part. Subfigures *a-b* show the median bioporosity observed in loam at the end of June 2019 and 2023, respectively. Subfigures *c-d* show the median bioporosity observed in sand at the end of June 2019 and 2023, respectively. The marginal increase in bioporosity in sand is partly because biopores collapsed in the sand, and remained stable only within the loam clods (subfigure *e*). Subfigures *f* and *g* shows the proportion of pores falling into defined diameter classes for loam and sand, respectively. The error bars denote the standard error ($n = 48$) and the shaded band around the regression line denote the confidence interval with $\alpha = 0.05$.

captured by the segmentation algorithm in the lower part for representative samples of loam (Fig. 3*a-b*) and sand (Fig. 3*c-d*). At the end of June 2019 for loam, the segmented biopores consisted of small isolated biopores that had persisted within the loam clods after the sieving procedure. They also consisted of some abiotic pores that were improperly classified as biopores (i.e., false positives) (Fig. 3*a*). At the end of June 2023, the captured biopores exhibited a large network of interconnected cylindrical structures (Fig. 3*b*). The biopores captured in June 2023 were thicker and more elongated than in June 2019. In sand, bioporosity in June 2019 was close to zero (Fig. 3*c*) and the increase in bioporosity in 2023 was only marginal (Fig. 3*d*). Visual inspection of the images provided evidence that the only persistent biopores in sand were the ones created in the more structurally stable loam clods present in the sand mixture (Fig. 3*e*).

The imprint of the maize root systems on the porous architecture of the soil could also be detected by changes in the pore size distribution in loam (Fig. 3*f*). The relative proportion of pores falling into the 25–125 μm diameter class was reduced from 74.02 ± 1.34 % to 55.08 ± 1.65 % between the end of June 2019 and March 2024 ($p < 0.001$). However, the relative proportion of pores falling into the 150–600 μm diameter class was increased from 24.20 ± 1.13 % to 37.32 ± 1.05 % ($p < 0.001$), and the relative proportion of pores falling into the 625–1350 μm diameter class was increased from 1.37 ± 0.39 % to 5.35 ± 0.69 % between the end of June 2019 and March 2024 ($p < 0.001$). In sand, there was no change in the pore size distribution between June 2019 and March 2024, for all three pore diameter classes considered (Fig. 3*g*). The relative proportion of pores falling into the 25–125 μm diameter class was 87.33 ± 0.39 % at the end of June 2019 and 85.37 ± 1.58 % in March 2024 ($p > 0.05$). The relative proportion of pores falling into the 150–600 μm diameter class was 12.62 ± 0.39 % at the end of June 2019 and 13.13 ± 0.47 % in March 2024 ($p > 0.05$). The relative proportion of pores falling into the 625–1350 μm diameter class was 1.37 ± 0.39 % at the end of June 2019 and was 0.68 ± 0.68 % in March 2024 ($p > 0.05$). Here also, there were no obvious differences in the pore size distribution between the maize *WT* and *rth3* genotypes, in both sand and loam (data not shown).

3.4. Volumetric water content and its impact on the visible porosity measurements

The volumetric water content varied significantly throughout the sampling events and showed the presence of "dry" and "wet" sampling events. For example, in March 2024, evapotranspiration in the early season was still low and the volumetric water content of loam ranged from 20.9 % to 30.1 %. In late June 2023, the volumetric water content of loam ranged from 17.7 % to 22.7 % only (Fig. 4*a*). Linear regression analyzes between the volumetric water content of the soil and the total visible porosity (Fig. 4*b*) revealed that differences in the volumetric water content affected the porosity measurements derived from X-ray CT (Fig. 4*c*). In fact, the higher the volumetric water content, the lower the visible porosity. This was true in loam (adj. $R^2 = 0.08$; $p < 0.001$) and in sand, but the effect was stronger in sand (adj. $R^2 = 0.23$; $p < 0.001$). The impact of soil volumetric water content on the bioporosity measurements was also significant for both sand (adj. $R^2 = 0.08$; $p < 0.001$) and loam (adj. $R^2 = 0.09$; $p < 0.001$) (Figure SM4).

3.5. Input of root-derived paticulate organic matter

The response of bioporosity development to soil texture could be interpreted with the root-derived POM differentiated in living roots or root residues (Fig. 5). In loam, the amount of root-derived POM remained relatively constant during the course of the experiment, with values ranging from 0.02 % to 0.17 % of the total volume (Fig. 5*a* to *h*). In sand, we observed a clear tendency to accumulate root residues. This manifested itself in a steady increase in root-derived POM over time (Fig. 5*i* to *p*). This accumulation was stronger at depths of 6.5 and 16.5 cm (Fig. 5*i-j-m-n*), compared to depths of 26.5 and 36.5 cm (Fig. 5*k-l-o-p*). In sand, the amount of root-derived POM ranged from 0.03 % to 0.41 % of the total volume. There were no differences in the amount of root-derived POM between the *WT* and *rth3* genotypes in sand ($p > 0.05$) and loam ($p > 0.1$), and this was true in any year. By combining both genotypes together, we found that the amount of root-derived POM in the sand was 1.9 times greater than in the loam at the end of June 2023 at 6.5 cm depth. For both loam and sand, the amount of living roots and root residues decreased with depth ($p < 0.001$).

Fig. 6 illustrates 3D renderings of root-derived POM for four representative soil samples extracted in loam and sand. In 2019, root residues were practically absent and living roots constituted most of the root-derived POM in both sand and loam (Fig. 6*a-c*). In 2023, living roots constituted most of the root-derived POM in loam (Fig. 6*b*), while root residues constituted most of the root-derived POM in sand (Fig. 6*d*).

4. Discussions

Our results demonstrate that soil texture was the main driver governing the development of soil structure and the fate of root-derived particulate organic matter in soils. In loam, plant roots degraded quickly and left behind a network of interconnected biopores. Most likely, this network of biopores observed with X-ray CT at the microscale (Fig. 3*b*) was responsible for an increase in infiltration capacity measured with tension infiltrometers at the macroscale (Fig. 1*c*). The observed increase in infiltration capacity as a result of root growth aligns well with the results of other authors (Wu et al., 2016; Yu et al., 2016; Meek et al., 1992), who also found a positive influence of vegetation cover on the infiltration capacity of fine-textured soils. The saturated hydraulic conductivity on the loam increased by a factor of 1.3 after five years of consecutive maize cultivation. However, this increase is much lower than the values typically reported in the literature, as differences usually amount to several orders of magnitude (Lu et al., 2020). This is probably explained by soil settlement, which simultaneously decreased infiltration capacity (Meek et al., 1992).

After five years of consecutive cultivation of maize on loam, the mean bioporosity increased from $0.06 \pm 9.8e^{-5}$ to $0.41 \pm 6.4e^{-4}$ % of the total volume at 6.5 cm depth. This value of 0.41 % of bioporosity is consistent with the value reported by Lucas et al. (2019b) for samples extracted at a mine reclamation site (with similar initial conditions) and scanned with X-ray CT at a resolution of 19 μm. Despite the fact that the reported value of Lucas et al. (2019b) is 2.4 times higher (0.98 %), the difference can be explained by the fact that (1) Lucas et al. (2019b) investigated a loess rich in calcium carbonate, for which the structural stability of the biopores was likely improved; (2) bioporosity was measured after six years of cultivation (versus five in our case), and (3) biopores in the first three years were created by Alfalfa (*Medicago sativa* L.), of which the root system is usually larger in size and grows deeper (Schoo et al., 2017). Unlike the data of Lucas et al. (2019b), our data do

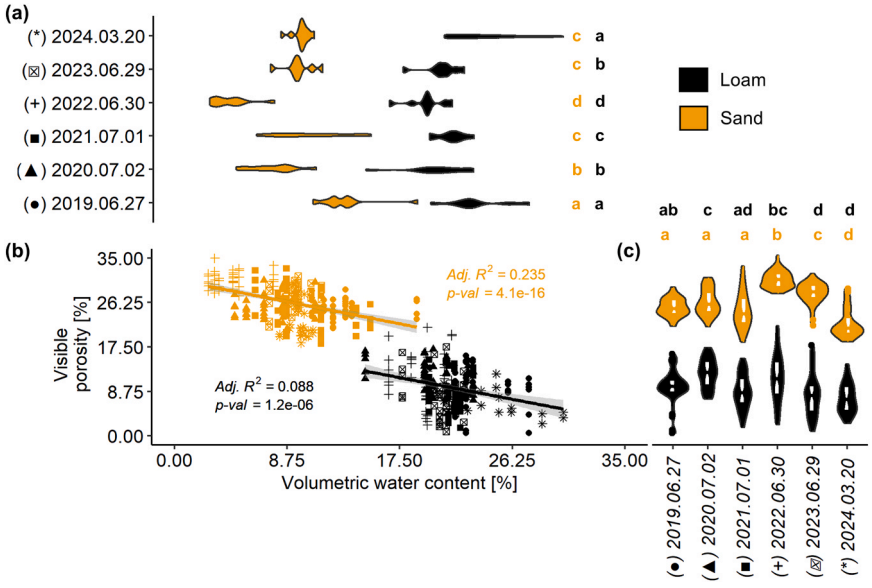

Fig. 4. Influence of the soil volumetric water content (subfigure *a*) on the visible porosity measured with X-ray CT (subfigure *c*). Subfigure *b* shows linear regressions between both metrics and indicates a stronger effect of the soil volumetric content on the visible porosity in sand, as compared to loam. The compact letters in subfigure *a* and *c* show the assignments of each sampling dates to statistical groups with a threshold value of $p < 0.05$. The symbols between parentheses preceding the labels of the x-axis of subfigure *a* and *c* link the dates of the sampling events with the symbols of subfigure *b*.

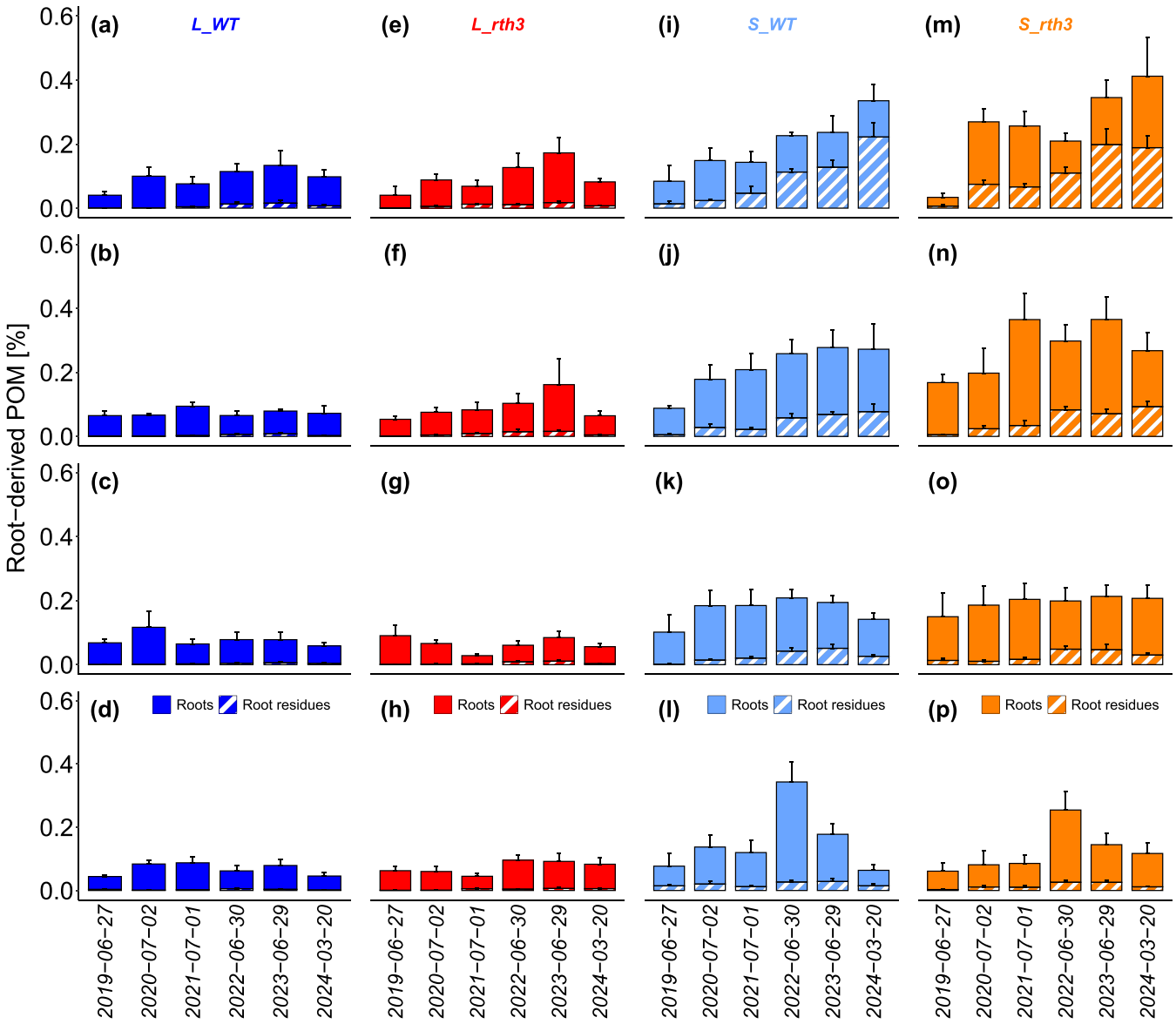

Fig. 5. Root-derived POM expressed in percentage of the total sample volume for the treatments *L_WT* (in blue; subfigures *a* to *d*), *L_rth3* (in red; subfigures *e* to *h*), *S_WT* (in light blue; subfigures *i* to *l*), and *S_rth3* (in orange; subfigures *m* to *p*). Subfigures are vertically ordered so as to reflect the sampled depths, i.e., subfigures *a*, *e*, *i* and *m* correspond to 6.5 cm depth, *b*, *f*, *j* and *n* correspond to 16.5 cm depth, *c*, *g*, *k* and *o* correspond to 26.5 cm depth, and *d*, *h*, *l* and *p* correspond to 36.5 cm depth. The error bars denote the standard error of the measurements around the mean value ($n = 6$). The plain filling patterns correspond to the root-derived POM contributed by the living roots, while the patterns with stripes correspond to the root-derived POM contributed by the root residues.

not show evidence that a dynamic equilibrium of bioporosity was reached after five years of consecutive maize cultivation. This is an indication that the roots were still predominantly creating new pores, instead of reusing existing ones.

In loam, root-induced biopores had a remarkable effect on soil pore size distribution (Figures 3*f-g*). In fact, maize roots created a shift from the smaller pore diameter classes to the larger diameter classes. This can be explained by the fact that, by growing in pores smaller than themselves, roots pushed away soil particles to the side and physically enlarged the soil pores (Lucas et al., 2019a, 2022; Phalempin et al., 2021b). This phenomenon is well documented in systems for which the physical disturbance of root-induced pores is absent, e.g., in zero-tillage systems (Wardak et al., 2022,2024). In this field experiment, most of the pores were at first irregularly shaped pores. However, after some time, the soil structure evolved to a root-dominated system (Scholl et al., 2014), typical of non-tilled systems. The temporal evolution of soil structure heterogeneity can also be appreciated in Fig. 2, most particularly for the 6.5 and 16.5 cm depths in loam (Fig. 2*a-b*). In fact, in 2019, bioporosity values were well contained within a narrow range; however, as soil heterogeneity developed, the spread of data points increased. The temporal evolution of soil structure heterogeneity can also be evaluated by comparing the spread of the bulk density measurements in 2019 and 2024 (Fig. 1*b*). In sand, soil structure heterogeneity barely developed between 2019 and 2024. This is supported not only by the narrow spread of bulk density values between 2019 and 2024 (Fig. 1*b*), but also by the constant frequency distribution of the pore diameter classes over the years (Fig. 3*g*).

As already highlighted by Lucas et al. (2022), soil fauna and plant roots are linked in multiple ways and their effects cannot be clearly separated without the use of unrealistic controls. In our study, we considered bioporosity as the normalized volume of root-induced empty channels. In reality, root-induced empty channels and pores induced by bioturbating animals are hard to distinguish because they usually share similar characteristics, that is, they are cylindrical and filled with air. In

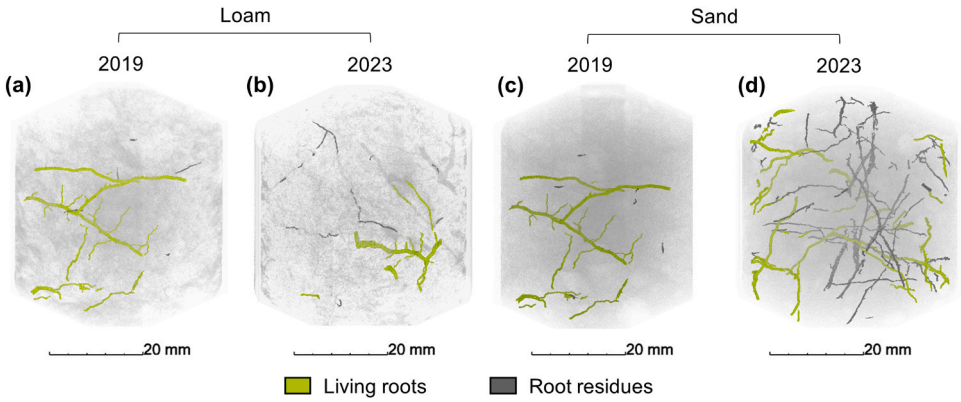

Fig. 6. Three-dimensional renderings of root-derived POM for four soil samples extracted in loam (subfigure *a* and *b*) and in sand (subfigure *c* and *d*), in June 2019 (subfigure *a* and *c*) and 2023 (subfigure *b* and *d*). Living roots are shown in green, whereas root residues are shown in gray. These samples have a root-derived POM content that is the closest to the median value observed in June 2019 and 2023, respectively.

our study, we cannot exclude the fact that soil fauna contributed to some increase in bioporosity; however, we can assume that its effect was likely minimal. In fact, it took quite some time for the soil fauna (e.g., earthworms) from the adjacent grassland to recolonize the repacked soil plots. As a result, only a few earthworm burrows (four in total) were observed in the images, and they were mostly observed in the samples extracted in 2023 and 2024. Due to the low abundance of soil fauna such as earthworms in our dataset, we decided not to introduce a class dedicated to it in the segmentation scheme because of a lack of representativeness.

By combining X-ray CT derived porosity and volumetric water content measurements, we could show that the volumetric water content affected the measured (bio-)porosity values. For example, during a wet sampling event, such as in March 2024, the measured (bio-)porosity values were lower than the values measured during dry sampling events, such as in June 2023 and 2022 (Fig. 2*a*). We postulate that this was the reflection of two concomitant effects. The first effect resulted from the swelling and shrinking behavior, that is, in a moist state, the soil tended to swell, which could close (bio-)pores and cracks, which would otherwise be detected as (bio-)pores in a drier moisture state. This effect was likely predominant in loam and absent in sand, as the clay content in sand was only 2.6 % (Table 1). The second effect resulted from the misassignment of the pore class when it is filled with water. When soil pores were filled with water, their X-ray attenuation coefficient became closer to the attenuation of the POM class or the soil matrix class with subresolution porosity. These water-filled pores could be falsely segmented as POM or soil matrix. Both effects are known to affect porosity measurements with X-ray CT imaging (Diel et al., 2019; Mooney et al., 2012), but are difficult to correct for. To correct for this effect, it would have been necessary to establish a relationship between volumetric water content and (bio-)porosity for each sample individually. This would have drastically increased the number of X-ray CT scans necessary. Alternatively, adjusting the volumetric water content of the cores prior to X-ray CT scanning was a possibility; however, it would have compromised the integrity of the root tissues. In fact, root degradation would have occurred during the time necessary to reach equilibrium between the imposed matric potential and the volumetric water content.

In sand, the amount of root-derived POM largely exceeded that of loam after five years (Fig.5). This higher POM content was the reflection of more vigorous root growth and larger root diameters in sand compared to loam (Vetterlein et al., 2022). It was also due to a lower rate of root decomposition in previous growing years, which caused an accumulation of root tissues. The reason for the slow decomposition of the roots was probably the low abundance of saprophytic microbes. In another study conducted within the same field experiment in 2023, Teixeira et al. found that the total phospholipid fatty acid concentration was approximately 3.5 times lower in sand, compared to loam ($p < 0.001$) (P. Teixeira, personal communication, 8 May 2024). Because the total concentration of phospholipid fatty acids reflects the biomass of living microbes, low concentrations generally indicate low microbial abundance and, often, low levels of activity in the soil (Frostegard and Baath, 1996). Another reason for the slow decomposition of root tissues was probably the low amount of organic carbon in the sand. At the beginning of the experiment, the soil organic carbon in the sand amounted to 0.15 % only, while it amounted to 0.85 % in the loam (Table 1). Because organic carbon in soil serves as the primary energy and carbon source for heterotrophic soil microbes, lower carbon availability can slow microbial metabolism, leading to decreased activity (Six et al., 2006). Most probably, the low amount of organic carbon and the low microbial abundance resulted in an accumulation of root-derived POM in the sand. The reason why roots and associated exudates (Santangeli et al., 2024) did not serve as potential substrates to trigger the soil microbiome is still not clear. Possibly, differences in root diameter, poor root-soil contact, C/N ratio or secondary metabolites played a role in slowing degradation.

The slow decomposition of roots in sand observed in this study was in good agreement with our previous study conducted under laboratory conditions using the same substrates (Phalempin et al., 2022). Previously, we found that root residues in the sand were still present after 216 days of incubation at 25 °C, while roots completely decomposed in loam after 78 days only. We further demonstrated that when the roots in sand fully decomposed, the biopores created tended to collapse (see Fig. 3c in Phalempin et al. 2022). In the present study, we did not monitor the structural stability of the biopores over time. However, visual inspection of the images provided evidence that the biopores collapsed in the sand, whereas they were stable in the loam clods embedded in the sand matrix (Fig. 3*e*). The fact that there was no increase in bioporosity with time in the sand at the lowest depths (Fig. 2*g-h*) was also a good indication that the biopores tended to collapse as a result of overburdening pressure and low structural stability. This observation is in good agreement with Schneider and Don (2019), who showed that the abundance of biopores was lower in coarse-textured soils.

Interestingly, the amount of living roots observed in March 2024 was still quite high (Fig. 5), despite the fact that the plots were bare at that time of year. In fact, visual inspection of the images showed that many root residues of the previous growing year (2023) were still detected as living roots, that is, their gray value range was higher than that of normal root residues (see figure SM1.4*c*). This suggests that microbial activity and associated root degradation was low during the winter 2023–2024. Possibly, a large part of the decomposition of root residues occured between March and June, when temperature and moisture were optimal (Akinremi et al., 1999; Kirschbaum, 1995). This hypothesis is supported by the results of Gelybó et al. (2022), who showed that soil

respiration is at its peak between April and June under temperate climate conditions in Europe. This hypothesis is also supported by the results of Xu and Qi (2001), who measured maximum and minimum CO_2 efflux at the end of May and in December, respectively, in a climate with cold and wet winter and warm and dry summer.

5. Conclusion

Our study highlighted the significant influence of soil texture on soil structure development driven by plant roots and the fate of root-derived particulate organic matter. In fine-textured soils with an organic carbon content similar to that of typical agricultural soils in a temperate European climate, roots rapidly decomposed and formed interconnected biopore networks. In contrast, in coarse-textured soils with a low organic carbon content typical of degraded soils or soils in arid regions, roots decomposed slower, leading to root necromass accumulation. These findings provide critical insight into the conditions that govern the formation and stabilization of organic matter.

Our findings further demonstrated that, in fine-textured and cohesive soils, the development of well-connected biopore networks at the microscale increased soil infiltration capacity at the macroscale. In contrast, in coarse-textured soils with low cohesive forces between soil particles, the biopores collapsed and root decay did not increase the infiltration capacity. These results emphasize the intricate relationship between soil structure, biotic factors such as root growth, and hydrological processes.

Our approach leveraged X-ray CT imaging of undisturbed soil cores and advanced machine learning segmentation methods to differentiate living roots from root residues. To our knowledge, this new segmentation procedure is an innovation in the field. This highlights that X-ray CT, in combination with powerful image processing tools, can be used to monitor the long-term evolution of soil structure dynamics. This has far-reaching implications for the quantitative analysis of soil structure and its linkage with soil functions in agroecosystems.

These insights underscore the need to integrate organic matter dynamics into soil structure studies, with important implications for sustainable land management and carbon storage strategies. Future research could expand these methods to diverse soil types and climatic conditions, in order to advance our ability to model soil processes and optimize soil management globally.

Funding

This project was carried out within the framework of the priority program 2089 “Rhizosphere spatiotemporal organisation - a key to rhizosphere functions” funded by DFG, German Research Foundation (Project no. 403801423).

CRediT authorship contribution statement

Steffen Schlüter: Writing – review & editing, Validation, Supervision, Resources, Project administration, Methodology, Funding acquisition, Conceptualization. **Doris Vetterlein:** Writing – review & editing, Supervision, Resources, Project administration, Funding acquisition, Conceptualization. **Ralf Gründling:** Writing – review & editing, Data curation. **Susanne Schreiter:** Writing – review & editing. **John Maximilian Köhne:** Writing – review & editing, Data curation. **Nils Jentzsch:** Writing – review & editing, Data curation. **Maxime Phalempin:** Writing – original draft, Visualization, Validation, Software, Methodology, Investigation, Formal analysis, Data curation.

Declaration of Competing Interest

The authors declare that they have no known competing financial interests or personal relationships that could have appeared to influence the work reported in this paper.

Data Availability

Data will be made available on request.

Acknowledgments

The authors thank Benjamin Pietzner, Sebastian Häusler and Eric Braatz for supporting the maintenance of the field experiment. We also acknowledge the contributions of many master students from the Martin-Luther University of Halle-Wittenberg who helped during the sampling events. In addition, we acknowledge Caroline Macron and Frank Hochholdinger (University Bonn) for providing the seeds for the maize genotypes *rth*3. Finally, we thank Florian Stoll, Jan Vanderborght, Osman Mustafa, Mathieu Javaux, Andrea Carminati and Mutez Ali Ahmed for collecting and sharing the volumetric water content data with us.

Appendix A. Supporting information

Supplementary data associated with this article can be found in the online version at doi:10.1016/j.still.2025.106561.

References

Akinremi, O., McGinn, S., McLean, H., 1999. Effects of soil temperature and moisture on soil respiration in barley and fallow plots. Can. J. Soil Sci. 79, 5–13.
Ankeny, M.D., Ahmed, M., Kaspar, T.C., Horton, R., 1991. Simple field method for determining unsaturated hydraulic conductivity. Soil Sci. Soc. Am. J. 55, 467–470.
Arzt, M., Deschamps, J., Schmied, C., Pietzsch, T., Schmidt, D., Tomancak, P., Haase, R., Jug, F., 2022. LABKIT: labeling and segmentation toolkit for big image data. Front. Comput. Sci. 4. https://doi.org/10.3389/fcomp.2022.777728.
Benjamini, Y., Hochberg, Y., 2018. Controlling the false discovery rate: a practical and powerful approach to multiple testing. J. R. Stat. Soc. B: Stat. Method. 57, 289–300. https://doi.org/10.1111/j.2517-6161.1995.tb02031.x.
Bleiholder, H., Weber, E., Lancashire, P., Feller, C., Buhr, L., Hess, M., Wicke, H., Hack, H., Meier, U., Klose, R., 2001. Growth stages of mono-and dicotyledonous plants, BBCH monograph. Fed. Biol. Res. Cent. Agric. For., Berl. /Braunschw. Ger. 158.
Cheik, S., Jouquet, P., Maeght, J.L., Capowiez, Y., Tran, T., Bottinelli, N., 2021. X-ray tomography analysis of soil biopores structure under wetting and drying cycles. Eur. J. Soil Sci. 72, 2128–2132. https://doi.org/10.1111/ejss.13119.
Diel, J., Vogel, H.J., Schlüter, S., 2019. Impact of wetting and drying cycles on soil structure dynamics. Geoderma 345, 63–71.
Doube, M., Kłosowski, M.M., Arganda-Carreras, I., Cordeliéres, F.P., Dougherty, R.P., Jackson, J.S., Schmid, B., Hutchinson, J.R., Shefelbine, S.J., 2010. Bonej: free and extensible bone image analysis in imagej. Bone 47, 1076–1079. https://doi.org/10.1016/j.bone.2010.08.023.
Dunn, O.J., 1964. Multiple comparisons using rank sums. Technometrics 6, 241–252.
Frostegård, A., Bååth, E., 1996. The use of phospholipid fatty acid analysis to estimate bacterial and fungal biomass in soil. Biol. Fertil. Soils 22, 59–65.
Gardner, W.R., 1958. Some steady-state solutions of the unsaturated moisture flow equation with application to evaporation from a water table. Soil Sci. 85, 228–232.
Gelybó, G., Barcza, Z., Dencső, M., Potyó, I., Kása, I., Horel, A., Pokovai, K., Birkás, M., Kern, A., Hollós, R., Tóth, E., 2022. Effect of tillage and crop type on soil respiration in a long-term field experiment on chernozem soil under temperate climate. Soil Tillage Res. 216, 105239. https://doi.org/10.1016/j.still.2021.105239.
Hou, L., Gao, W., der Bom, F., Weng, Z., Doolette, C.L., Maksimenko, A., Hausermann, D., Zheng, Y., Tang, C., Lombi, E., Kopittke, P.M., 2022. Use of x-ray tomography for examining root architecture in soils. Geoderma 405, 115405. https://doi.org/10.1016/j.geoderma.2021.115405.
Jorda, H., Ahmed, M.A., Javaux, M., Carminati, A., Duddek, P., Vetterlein, D., Vanderborght, J., 2022. Field scale plant water relation of maize (Zea mays) under drought - impact of root hairs and soil texture. Plant Soil 478, 59–84. https://doi.org/10.1007/s11104-022-05685-x.
Kautz, T., 2015. Research on subsoil biopores and their functions in organically managed soils: A review. Renew. Agric. Food Syst. 30, 318–327. https://doi.org/10.1017/S1742170513000549.
Keller, T., Colombi, T., Ruiz, S., Schymanski, S.J., Weisskopf, P., Koestel, J., Sommer, M., Stadelmann, V., Breitenstein, D., Kirchgessner, N., Walter, A., Or, D., 2021. Soil structure recovery following compaction: short-term evolution of soil physical properties in a loamy soil. Soil Sci. Soc. Am. J. 85, 1002–1020. https://doi.org/10.1002/saj2.20240.
Kirschbaum, M.U.F., 1995. The temperature dependence of soil organic matter decomposition, and the effect of global warming on soil organic c storage. Soil Biol. Biochem. 27, 753–760. https://doi.org/10.1016/0038-0717(94)00242-S.
König, S., Weller, U., Betancur-Corredor, B., Lang, B., Reitz, T., Wiesmeier, M., Wollschläger, U., Vogel, H.J., 2023. BODIUM—a systemic approach to model the dynamics of soil functions. Eur. J. Soil Sci. 74, e13411. https://doi.org/10.1111/ejss.13411.

Kruskal, W.H., Wallis, W.A., 1952. Use of ranks in one-criterion variance analysis 47, 583–621. https://doi.org/10.1080/01621459.1952.10483441.
Leuther, F., Schlüter, S., 2021. Impact of freeze-thaw cycles on soil structure and soil hydraulic properties. Soil 7, 179–191.
Lu, J., Zhang, Q., Werner, A.D., Li, Y., Jiang, S., Tan, Z., 2020. Root-induced changes of soil hydraulic properties - a review. J. Hydrol. 589, 125203. https://doi.org/10.1016/j.jhydrol.2020.125203.
Lucas, M., Schlüter, S., Vogel, H.J., Vetterlein, D., 2019a. Roots compact the surrounding soil depending on the structures they encounter. Sci. Rep. 9, 1–13. https://doi.org/10.1038/s41598-019-52665-w.
Lucas, M., Schlüter, S., Vogel, H.J., Vetterlein, D., 2019b. Soil structure formation along an agricultural chronosequence. Geoderma 350, 61–72. https://doi.org/10.1016/j.geoderma.2019.04.041.
Lucas, M., Nguyen, L.T.T., Guber, A., Kravchenko, A.N., 2022. Cover crop influence on pore size distribution and biopore dynamics: enumerating root and soil faunal effects. Front. Plant Sci. 13. https://doi.org/10.3389/fpls.2022.928569.
Mann, H.B., Whitney, D.R., 1947. On a test of whether one of two random variables is stochastically larger than the other. Ann. Math. Stat. 18, 50–60. https://doi.org/10.1214/aoms/1177730491.
Meek, B.D., Rechel, E., Carter, L.M., DeTar, W.R., Urie, A., 1992. Infiltration rate of a sandy loam soil: effects of traffic, tillage, and plant roots. Soil. Sci. Soc. Am. J. 56, 908–913.
Meurer, K., Barron, J., Chenu, C., Coucheney, E., Fielding, M., Hallett, P., Herrmann, A. M., Keller, T., Koestel, J., Larsbo, M., Lewan, E., Or, D., Parsons, D., Parvin, N., Taylor, A., Vereecken, H., Jarvis, N., 2020. A framework for modelling soil structure dynamics induced by biological activity. Glob. Change Biol. 26, 5382–5403. https://doi.org/10.1111/gcb.15289.
Mooney, S.J., Pridmore, T.P., Helliwell, J., Bennett, M.J., 2012. Developing x-ray computed tomography to non-invasively image 3-d root systems architecture in soil. Plant Soil 352, 1–22.
Morel, J.L., Habib, L., Plantureux, S., Guckert, A., 1991. Influence of maize root mucilage on soil aggregate stability. Plant Soil 136, 111–119.
Mueller, C.W., Baumert, V., Carminati, A., Germon, A., Holz, M., Kögel-Knabner, I., Peth, S., Schlüter, S., Uteau, D., Vetterlein, D., Teixeira, P., Vidal, A., 2024. From rhizosphere to detritusphere - soil structure formation driven by plant roots and the interactions with soil biota. Soil Biol. Biochem. 193, 109396. https://doi.org/10.1016/j.soilbio.2024.109396.
Or, D., Keller, T., Schlesinger, W.H., 2021. Natural and managed soil structure: on the fragile scaffolding for soil functioning. Soil Tillage Res 208, 104912. https://doi.org/10.1016/j.still.2020.104912.
Phalempin, M., Lippold, E., Vetterlein, D., Schlüter, S., 2021b. Soil texture and structure heterogeneity predominantly governs bulk density gradients around roots. Vadose Zone J. 20, e20147. https://doi.org/10.1002/vzj2.20147.
Phalempin, M., Lippold, E., Vetterlein, D., Schlüter, S., 2021a. An improved method for the segmentation of roots from x-ray computed tomography 3d images: Rootine v. 2. Plant Methods 17, 1–19. https://doi.org/10.1186/s13007-021-00735-4.
Phalempin, M., Landl, M., Wu, G.M., Schnepf, A., Vetterlein, D., Schlüter, S., 2022. Maize root-induced biopores do not influence root growth of subsequently grown maize plants in well aerated, fertilized and repacked soil columns. Soil Tillage Res 221, 105398. https://doi.org/10.1016/j.still.2022.105398.
QGIS Development Team, 2023.QGIS Geographic Information System.⟨https://qgis.org⟩. open Source Geospatial Foundation Project.
R Core Team, 2024.R: A Language and Environment for Statistical Computing. R Foundation for Statistical Computing. Vienna, Austria.⟨https://www.R-project.org/⟩.
Rabot, E., Wiesmeier, M., Schlüter, S., Vogel, H.J., 2018. Soil structure as an indicator of soil functions: A review. Geoderma 314, 122–137. https://doi.org/10.1016/j.geoderma.2017.11.009.
Redmile-Gordon, M., Gregory, A.S., White, R.P., Watts, C.W., 2020. Soil organic carbon, extracellular polymeric substances (eps), and soil structural stability as affected by previous and current land-use. Geoderma 363, 114143. https://doi.org/10.1016/j.geoderma.2019.114143.
Sandin, M., Koestel, J., Jarvis, N., Larsbo, M., 2017. Post-tillage evolution of structural pore space and saturated and near-saturated hydraulic conductivity in a clay loam soil. Soil Tillage Res. 165, 161–168. https://doi.org/10.1016/j.still.2016.08.004.
Santangeli, M., Steininger-Mairinger, T., Vetterlein, D., Hann, S., Oburger, E., 2024. Maize (Zea mays l.) root exudation profiles change in quality and quantity during plant development - a field study. Plant Sci. 338, 111896. https://doi.org/10.1016/j.plantsci.2023.111896.
Schädler, M., Buscot, F., Klotz, S., Reitz, T., Durka, W., Bumberger, J., Merbach, I., Michalski, S.G., Kirsch, K., Remmler, P., Schulz, E., Auge, H., 2019. Investigating the consequences of climate change under different land-use regimes: a novel experimental infrastructure. Ecosphere 10, e02635. https://doi.org/10.1002/ecs2.2635.
Schindelin, J., Arganda-Carreras, I., Frise, E., Kaynig, V., Longair, M., Pietzsch, T., Preibisch, S., Rueden, C., Saalfeld, S., Schmid, B., 2012. Fiji: an open-source platform for biological-image analysis. Nat. Methods 9, 676–682. https://doi.org/10.1038/nmeth.2019.
Schneider, F., Don, A., 2019. Root-restricting layers in german agricultural soils. part ii: Adaptation and melioration strategies. Plant Soil 442, 419–432. https://doi.org/10.1007/s11104-019-04186-8.
Scholl, P., Leitner, D., Kammerer, G., Loiskandl, W., Kaul, H.P., Bodner, G., 2014. Root induced changes of effective 1d hydraulic properties in a soil column. Plant Soil 381, 193–213. https://doi.org/10.1007/s11104-014-2121-x.
Schoo, B., Schroetter, S., Kage, H., Schittenhelm, S., 2017. Root traits of cup plant, maize and lucerne grass grown under different soil and soil moisture conditions. J. Agron. Crop Sci. 203, 345–359. https://doi.org/10.1111/jac.12194.
Schwen, A., Bodner, G., Loiskandl, W., 2011. Time-variable soil hydraulic properties in near-surface soil water simulations for different tillage methods. Agric. Water Manag. 99, 42–50. https://doi.org/10.1016/j.agwat.2011.07.020.
Six, J., Frey, S.D., Thiet, R.K., Batten, K.M., 2006. Bacterial and fungal contributions to carbon sequestration in agroecosystems. Soil Sci. Soc. Am. J. 70, 555–569. https://doi.org/10.2136/sssaj2004.0347.
Uteau, D., Pagenkemper, S.K., Peth, S., Horn, R., 2013. Root and time dependent soil structure formation and its influence on gas transport in the subsoil. Soil Tillage Res. 132, 69–76. https://doi.org/10.1016/j.still.2013.05.001.
Vetterlein, D., Carminati, A., Kögel-Knabner, I., Bienert, G.P., Smalla, K., Oburger, E., Schnepf, A., Banitz, T., Tarkka, M.T., Schlüter, S., 2020. Rhizosphere spatiotemporal organization-a key to rhizosphere functions. Front. Agron. 2. https://doi.org/10.3389/fagro.2020.00008.
Vetterlein, D., Lippold, E., Schreiter, S., Phalempin, M., Fahrenkampf, T., Hochholdinger, F., Marcon, C., Tarkka, M., Oburger, E., Ahmed, M., Javaux, M., Schlüter, S., 2021. Experimental platforms for the investigation of spatiotemporal patterns in the rhizosphere—laboratory and field scale. J. Plant Nutr. Soil Sci. 184, 35–50. https://doi.org/10.1002/jpln.202000079.
Vetterlein, D., Phalempin, M., Lippold, E., Schlüter, S., Schreiter, S., Ahmed, M.A., Carminati, A., Duddek, P., Jorda, H., Bienert, G.P., Bienert, M.D., Tarkka, M., Ganther, M., Oburger, E., Santangeli, M., Javaux, M., Vanderborght, J., 2022. Root hairs matter at field scale for maize shoot growth and nutrient uptake, but root trait plasticity is primarily triggered by texture and drought. Plant Soil 478, 119–141. https://doi.org/10.1007/s11104-022-05434-0.
Wardak, D.L.R., Padia, F.N., de Heer, M.I., Sturrock, C.J., Mooney, S.J., 2022. Zero tillage has important consequences for soil pore architecture and hydraulic transport: a review. Geoderma 422, 115927. https://doi.org/10.1016/j.geoderma.2022.115927.
Wardak, D.L.R., Padia, F.N., de Heer, M.I., Sturrock, C.J., Mooney, S.J., 2024. Zero-tillage induces significant changes to the soil pore network and hydraulic function after 7 years. Geoderma 447, 116934. https://doi.org/10.1016/j.geoderma.2024.116934.
Weller, U., Albrecht, L., Schlüter, S., Vogel, H.J., 2022. An open soil structure library based on x-ray ct data. SOIL 8, 507–515. https://doi.org/10.5194/soil-8-507-2022 (sOIL).
Whalley, W.R., Dumitru, E., Dexter, A.R., 1995. Biological effects of soil compaction. Soil Tillage Res. 35, 53–68. https://doi.org/10.1016/0167-1987(95)00473-6.
Wickham, H., Navarro, D., Pedersen, T.L., 2023. ggplot2: Elegant Graphics for Data Analysis. Springer-Verlag, New York. ⟨https://ggplot2.tidyverse.org⟩.
Wooding, R.A., 1968. Steady infiltration from a shallow circular pond. Water Resour. Res. 4, 1259–1273. https://doi.org/10.1029/WR004i006p01259.
Wu, G.L., Yang, Z., Cui, Z., Liu, Y., Fang, N.F., Shi, Z.H., 2016. Mixed artificial grasslands with more roots improved mine soil infiltration capacity. J. Hydrol. 535, 54–60. https://doi.org/10.1016/j.jhydrol.2016.01.059.
Xu, M., Qi, Y., 2001. Soil-surface co2 efflux and its spatial and temporal variations in a young ponderosa pine plantation in northern california. Glob. Change Biol. 7, 667–677. https://doi.org/10.1046/j.1354-1013.2001.00435.x.
Young, I.M., Blanchart, E., Chenu, C., Dangerfield, M., Fragoso, C., Grimaldi, M., Ingram, J., Monrozier, L.J., 1998. The interaction of soil biota and soil structure under change. Glob. Change Biol. 4, 703–712. https://doi.org/10.1046/j.1365-2486.1998.00194.x.
Yu, Y., Loiskandl, W., Kaul, H.P., Himmelbauer, M., Wei, W., Chen, L., Bodner, G., 2016. Estimation of runoff mitigation by morphologically different cover crop root systems. J. Hydrol. 538, 667–676. https://doi.org/10.1016/j.jhydrol.2016.04.060.